Trends in Chemistry

CellPress REVIEWS

Review

# Building Brain-Inspired Logic Circuits from Dynamically Switchable Transition-Metal Oxides

Justin L. Andrews,[1,2] David A. Santos,[1,2] M. Meyyappan,[3] R. Stanley Williams,[4] and Sarbajit Banerjee[1,2,*,@]

**Processing, storing, and transmitting information accounts for ~10% of global energy use; projections suggest that computational energy demands will be 10× higher than the projected global energy supply by 2040. Realizing solid-state analogs of neural circuitry, using 'neuromorphic' materials, holds promise for enabling a new energy-efficient computing paradigm. The metal–insulator transitions (MITs) of electron-correlated transition-metal oxides provide an attractive vector for achieving large conductance switching with minimal energy dissipation. Here, we review current understanding of the mechanisms underpinning electronic instabilities, discuss methods for modulation of spiking behavior through tuning of atomistic and electronic structure, and highlight the need for establishing deterministic and independent control of transformation characteristics such as switching magnitude, energy thresholds, heat dissipation, hysteresis, and dynamics of relaxation.**

## Highlights

The metal–insulator transitions of electron-correlated transition-metal oxides provide a remarkably sensitive and versatile vector for achieving large conductance switching with minimal energy dissipation. Such materials have been amenable to being fashioned into neuroemulative circuits.

Capturing the complexity of neurons requires independent control over multiple transformation characteristics: the magnitude and energy threshold of conductance switching, heat dissipation, switching time, relaxation dynamics, and number of accessible internal states.

$RENiO_3$ and $M_xV_2O_5$ represent promising materials with expansive chemical design spaces and the potential for independent control of transformation characteristics.

## Brain-like Computing with Transition-Metal Oxides

The primary driver of the electronics revolution of the past 40 years, the exponential improvement in silicon integrated circuits with time (known as Moore's scaling), has saturated. This has occurred just as the era of 'big data' has arrived. We are now collecting more data than we can transmit, store, and analyze. Projections suggest that the demand for computation would be 10× higher than the projected global energy supply can support by 2040 [1]. Without exponential increases in computing power and efficiency, transformative visions such as the Internet of Things, autonomous transportation, and personalized medicine will be throttled by the inability of current computing technologies to handle the magnitude and complexity of human- and machine-generated data. The energy inefficiency of existing computing architectures derives from the fundamental constraints imposed by the physics of thermionic excitation of charge carriers across semiconductor conduction channels (Figure 1A) [2–4]. This translates to power demand and accompanying heat dissipation that no longer decrease with reduction in the size of active elements; in the modern 'age of dark silicon', a significant fraction of the chip must be left inoperative as a result of insurmountable power constraints [3].

The human brain processes complex information at least $10^4$ times more efficiently than digital computing on silicon [5,6]. Neurons combine information received across synaptic connections with many other dendrites and encode output information through specifically timed transsynaptic pulses, called 'action potentials.' Figure 1B shows the famous measurement by Hodgkin and Huxley across a giant squid axon [7]. Specific spike timings further enable the retention of multiple internal states (constituting memory), imbuing the ability to 'learn' through the evolution of internal neuronal weights [8]. Thus, unlike currently utilized **von Neumann architectures** (see Glossary), computing and memory functions are colocated in the human brain, enabling improved energy efficiency and reducing the need to shuttle data.

[1]Department of Chemistry, Texas A&M University, College Station, TX 77843, USA
[2]Department of Materials Science and Engineering, Texas A&M University, College Station, TX 77843, USA
[3]NASA Ames Research Center, Moffett Field, CA 94035, USA
[4]Department of Electrical and Computer Engineering, Texas A&M University, College Station, TX 77843, USA

*Correspondence: banerjee@chem.tamu.edu (S. Banerjee).
@Twitter: @SarbajitBanerj1 (S. Banerjee).

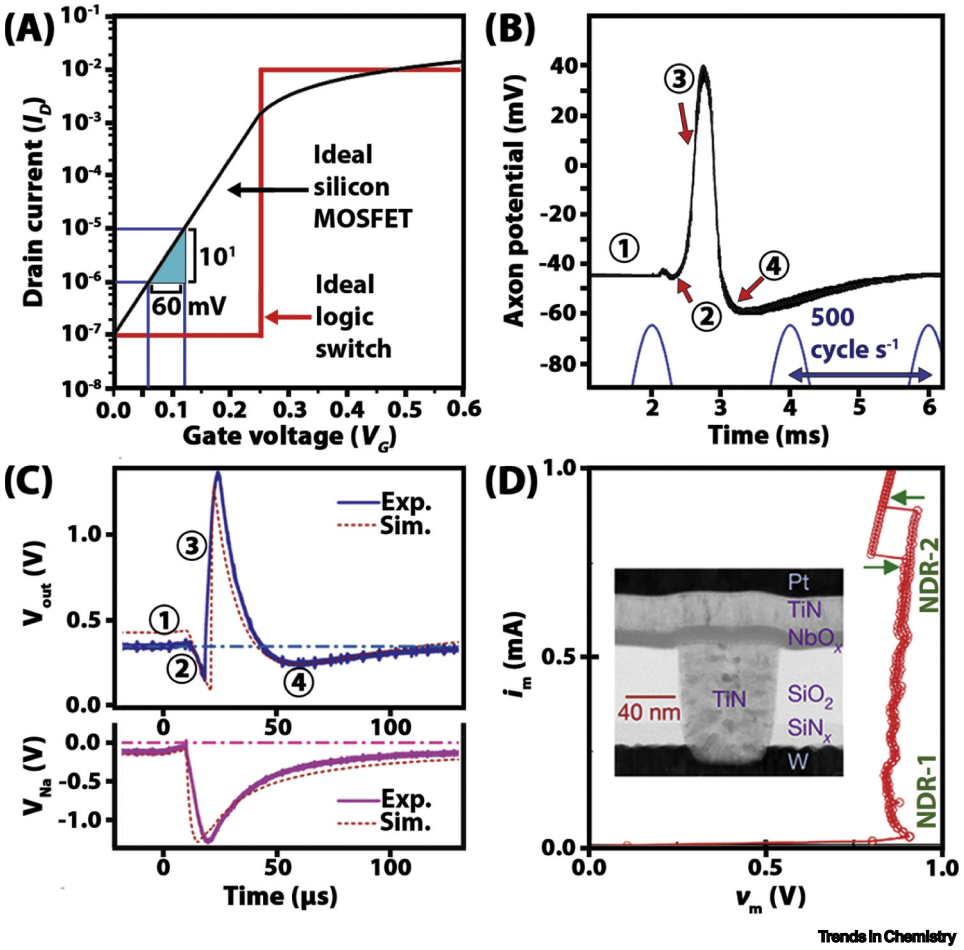


Figure 1. Contrasting Biological and Electronic Circuits. (A) Switching characteristics of workhorse silicon-based metal-oxide semiconductor field-effect transistors (MOSFETs) are shown in black; the Fermi–Dirac electron distribution of electron energies at room temperature limits the steepness of switching characteristics to 60 mV ($V_G$) per decade increase in current ($I_D$) across the transistor channel. Such characteristics embody the inefficiencies of digital computing [4]. An ideal logic switch with a much sharper slope is shown in red. (B) Action potential of a giant squid axon as originally recorded by Huxley and Hodgkin ('digitally remastered' using graph-digitizer software). Four distinct regions of the action potential are highlighted, comprising: (1) resting potential; (2) sodium-channel-driven hyperpolarization; (3) potassium-channel-driven depolarization; and (4) a refractory recovery period. (C) Neuromorphic action potential generated using a vanadium dioxide ($VO_2$) memristor maps to the biological action potential in (B) with high fidelity. This neuromorphic function is underpinned by the metal–insulator transition (MIT) of $VO_2$ and derives from the negative differential resistance (NDR) of the device. (D) Demonstration of NDR in a niobium dioxide ($NbO_2$) device. (B,C,D) adapted from [6,7,14], respectively.

## Emulating Neuronal Circuitry Using Physical Devices

Neuromorphic computing aims to design logic circuity that emulates neuronal logic and memory function. The possibility of emulating neuronal function using theorized circuit elements named **'neuristors'** was first proposed in 1962, but full realization of such a notion necessitates switching of the electrical conductance of solid-state compounds across orders of magnitude in an energy-efficient manner [9]. Initial approaches to neuromorphic computing utilized standard digital processors but were wasteful in terms of silicon area and power dissipation. Consequently, the next advance was to design new silicon-based chip architectures such as **complementary metal-oxide semiconductors (CMOSs)** explicitly for neural network applications [10,11],

## Glossary

**Complementary metal-oxide semiconductor (CMOS):** a type of integrated circuit in which p- and n-channel MOSFET transistors are fabricated in close proximity on the same silicon substrate.

**Hubbard '*U*':** the on-site Coulombic interaction between localized electrons; alternatively defined as the energy differential between the occupied (lower) and unoccupied (upper) Hubbard band.

**Leaky integrate-and-fire (LIF) neuron:** a model that attempts to account for neuronal dynamics, comprising: (i) a linear differential equation to account for dynamical summation/integration of the membrane potential over time; and (ii) a well-defined threshold, which, when crossed, triggers a firing event.

**Memristor:** a nonlinear circuit element whose internal electrical resistance captures not just the present state of the system but also its history.

**Mott–Hubbard bands:** strong electron correlation results in splitting of half-filled bands and concomitant destabilization of upper unoccupied states (UH band) and stabilization of lower occupied states (LH band).

**Mott transition:** an abrupt electronic transition between a metallic and a nonmetallic state whereby electrons become localized in specific bands, resulting in diminished conductivity; the Mott transition marks a tipping point between the kinetic energy gained by delocalizing an electron across a band and the potential energy penalty extracted by the Coulombic repulsion between electrons.

**Negative-charge-transfer insulator:** a class of charge-transfer insulators wherein the effective charge-transfer energy is less than 0 ($\Delta_{eff} < 0$) due to overlap of occupied ligand p states and unoccupied transition metal d states. The overlap of these states often leads to hybridization and the formation of a p/d–p/d pseudogap.

**Negative differential resistance (NDR):** across some regions of a current–voltage curve, current decreases as voltage increases (i.e., $dV/dI < 0$); NDR can be either voltage controlled ('N'-type) or current controlled ('S'-type) as is the case for $NbO_2$ in Figure 1D.

**Neuristor:** a device first proposed by Hewitt Crane in the 1960s that represents the simplest possible

seeking to mimic the **leaky integrate-and-fire (LIF)** behavior of neurons [12,13]. Nevertheless, these attempts have failed to approach the energy efficiency of the human brain and are constrained by the thermodynamic limitations of free-carrier-generation mechanisms in electrostatically modulated semiconductors (Figure 1A). Another key limitation of neuronal architectures emulated on conventional chips is their inability to mimic the chaotic current dynamics observed in biological counterparts, which are key to the success of the latter in pattern recognition [6,14,15].

### A Better Way to Emulate Neurons in the Solid State

For the abovementioned reasons, there is a clear need to design solid-state compounds that exhibit sharp spiking behavior characteristic of neurons; however, the palette of functional materials that exhibit intrinsic switchability of conductance to perform 'brain-like' computing tasks is sparse [16]. Emulating the complexity and diversity of neuronal characteristics requires independent control of multiple functional attributes of electronic phase transformations, including the magnitude and energy threshold of conductance switching, heat dissipation, hysteresis, the dynamics of relaxation between states, and the number of accessible internal states [6,17–25]. Recent demonstrations illustrate that electronic transitions within strongly correlated materials can be leveraged to emulate biological neurons (Figure 1C) [6,14,20]. These neuroemulative capabilities are underpinned by the tendency of such materials to manifest solid–solid metal-insulator transitions (MITs) in response to specific external stimuli such as temperature ($T_C$) or applied electric field. As exemplified in Figure 1D for niobium dioxide ($NbO_2$), MITs represent an energy-efficient class of 'memristive' behavior, where the resistance value at a given point in time captures both the present state of the system and its history, reflecting the capacity to evolve and learn [6,24,26]. Despite these recent successes [6,14,20], independent control of transformation characteristics remains to be established [17,27]. For instance, $NbO_2$ has too high a transition temperature (~1080 K) and thus consumes too much power [14,15,26], whereas vanadium dioxide ($VO_2$) has a transition temperature that is too low (~340 K) given the ~400-K operating temperatures of modern computing architectures [6]. Here, four classes of MIT materials are discussed: $VO_2$; $NbO_2$; rare-earth nickelates ($RENiO_3$); and ternary vanadium oxides ($M_XV_2O_5$) [6,14,16,20]. In particular, we focus on exploring means of *a priori* design of free-energy landscapes (e.g., the landscape depicted in Figure 3D) to enable switching function depicted for the materials included in Figure 2D, Key Figure [28,29].

## Unstable by Design: Electronic Transitions in Correlated Oxides

In strongly electron-correlated materials, electrons can no longer be considered as noninteracting, giving rise to complex many-body phenomena manifested as close coupling of structural, electronic, and spin degrees of freedom [16,30–36]. This often gives rise to materials that have localized charge carriers in the ground state but are at the cusp of transitioning to an itinerant state following: (i) structural transformations that alter the chemical bonding and degree of hybridization; or (ii) an increase in charge carrier density (e.g., through the application of an electric field, through thermal broadening of occupied Hubbard bands) such that electron–electron repulsions are screened. In contrast to systems where long-range ion diffusion or filament formation/dissolution underpins neuromorphic function [17,37], correlated oxides can exhibit relatively subtle structural transformations, resulting in intrinsically lower entropy production and thereby greater energy efficiency. The relative contributions of lattice distortions and electron correlation within such systems determine the energetic costs of transformations and govern the accessible dynamics. Electronic transitions within such compounds can be considered to derive from a convolution of structural (Peierls) and electronic (Mott) origins (Figure 2). In the Peierls case (Figure 2A), the equivalent of a dimerization gives rise to the improved overlap of electronic states across adjacent metal centers [38,39]. In the case of Mott insulators (Figure 2B), Coulombic repulsion

configuration capable of capturing the quintessential properties of a neuron, including integration of input signals and subsequent spiking above a 'learned' threshold.

**Peierls' transition:** a type of structural transition deriving from Peierls' theorem, which reasons that a 1D chain of equally spaced ions with one free valence electron each is unstable; as a consequence, the ions form dimers to lower the total energy of the system.

**von Neumann architecture:** the workhorse of modern computing comprising spatially separated central processing, memory, and input/output elements.

## Key Figure

### A Mechanistic View of Electronic Instabilities

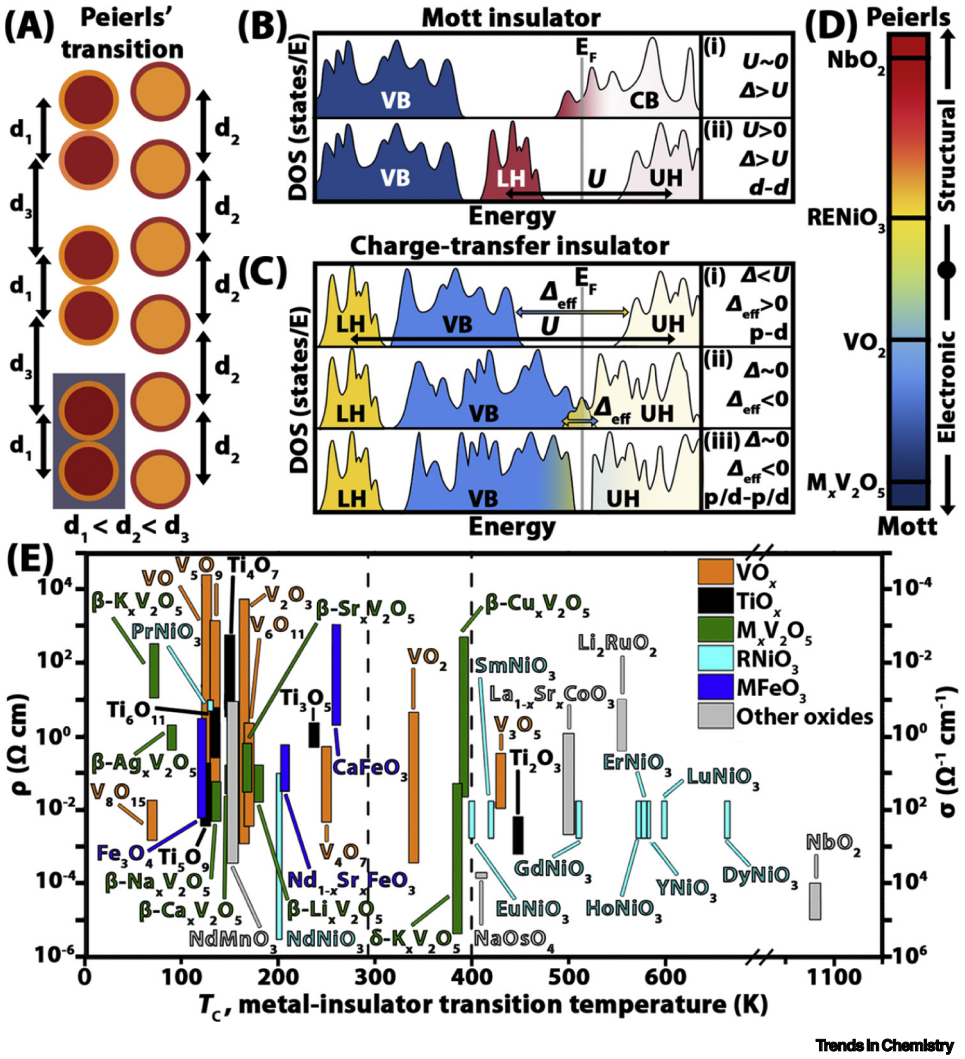


Figure 2. Metal–insulator transitions (MITs) can be conceptualized to arise from a weighted coupling of structural (i.e., Peierls) distortions and electronic (i.e., Mott) instabilities. (A) Schematic representation of a **Peierls' transition** driven by dimerization of adjacent metal centers. (B) An example of a Mott-type transition where electron correlation (*U*) gives rise to upper (UH) and lower (LH) Hubbard bands. (C) An example of an electronic transition wherein increased transition metal 3d–O 2p hybridization at high temperature results in the closing of a p/d–p/d quasigap, as reported for rare-earth nickelates [41]. Panel (ii) provides a notional illustration of negative charge transfer before correlation drives opening of the p/d-p/d quasi-gap. (D) Representation of the Mott-to-Peierls spectrum that describes the mechanistic origin of MITs in the materials discussed here. (E) Graphical representation of the MIT behavior of several correlated oxide materials; the horizontal axis shows MIT temperatures ($T_C$) and the vertical axes show reported changes in resistivity and conductivity. The height of each floating bar corresponds to the change in resistivity/conductivity between the metallic (bottom) and insulating (top) phases. Note that the change in resistivity for $RENiO_3$ materials to the right of samarium nickelate ($SmNiO_3$) is held constant since, in the absence of high-quality crystals, the achievable magnitudes of conductance switching remain to be determined [30]. Vertical lines at room temperature (298 K) and at the typical operating temperature of a computing unit (~400 K) are shown. A break in the x-axis (650–1050 K) is further included in light of the sparse examples in this range. Data shown in (E) collated from [21–23,25,42,45–53,111].

between electrons causes splitting of a half- or partially filled band into an upper Hubbard (UH) and a lower Hubbard (LH) band separated by the **Hubbard '*U*'**, defining an energy gap proportional to the on-site electrostatic repulsion and thereby lowering the overall energy of the system [16]. For Mott–Hubbard insulators, when the width of the Hubbard bands is less than $U$ (as is the case in the ground state), insulating behavior is observed. Alternatively, when the width is greater than $U$, metallic behavior is observed. In purely electronic transitions, broadening of Hubbard bands can be affected through thermal broadening of the bandwidth [21,23] or the introduction of additional charge carriers that screen repulsive interactions [40]. Mott insulators are distinguished from charge-transfer insulators by the nature of their bandgap. In charge-transfer insulators, the LH band is situated below the ligand p-band ($U > \Delta$, the crystal field splitting) and the effective bandgap (charge-transfer energy, $\Delta_{eff}$) is between the upper edge of the ligand p band and the lower edge of the unoccupied metal d band (for $\Delta_{eff} > 0$) or between correlation-split p/d hybridized states (for $\Delta_{eff} < 0$) (Figure 2C) [41,42]. Closing of the p–d or p/d–p/d gaps induced through alteration of bandwidths or filling of the bands and concomitant shifting of the Fermi level provides a means of inducing a MIT.

Although MITs have been evaluated in transition-metal chalcogenides, these materials tend to rely on electric field pulses and show degradation under field stress [12,43,44]. Their quasi-2D electronic structure nevertheless holds potential for establishing deterministic control of conduction pathways through surface functionalization. In this review, we focus on transition-metal oxides, which offer improved robustness and better compatibility with foundry processes, in addition to an extensive phase space where the extent of hybridization (bandwidths, overlap integrals) can be readily tuned [16,21–23,25,42,45–53]. The four materials classes discussed here have been approximately positioned along a 'Mott–Peierls spectrum' in Figure 2D, albeit that their specific positioning along this spectrum is not without controversy. This illustration highlights increasing realization of the importance of coupling between ionics, subtle structural distortions, and electron correlation in driving MITs. The massive phase space occupied by strongly correlated oxide materials is reflected in Figure 2E, which relays the critical transition temperatures ($T_C$) and the changes in resistivity of representative oxide materials. Many materials exhibit $T_C < 200$ K, a sparse few near-room temperature, and still fewer above the 400-K threshold imperative for computing. The lack of materials with $T_C > 400$ K underscores the need for mechanistic understanding and design of correlated systems. The four classes discussed here (Figure 2D) have been selected from among those shown in Figure 2E for the diversity of their MIT mechanisms, for recent demonstrations of their use as memory elements for brain-like computing, and for exhibiting compositional tunability of switching characteristics.

## The Binary Oxides of Vanadium and Niobium

$VO_2$ and $NbO_2$ represent model MIT materials well separated along the Mott–Peierls spectrum with respect to the MIT mechanism (Figure 2D) and furthermore exhibit vastly different transition temperatures (Figure 2E) [54]. The structural instability underpinning the MIT in $VO_2$ spans a complex phase space (Figure 3D) [19,28,55,56]. Around $T_C = 340$ K, $VO_2$ undergoes a first-order diffusionless phase transformation from a high-symmetry rutile-type phase (>340 K) to one of several stable ($M_1$) or metastable ($M_2$/$M_3$) low-symmetry phases (<340 K), as shown in Figure 3A. The high-temperature rutile phase exhibits a singular V–V bond distance (2.851 Å), which is distinguished from the low-temperature phase that is characterized by V–V dimers, with alternating long (3.125 Å)–short (2.654 Å) bonds ($M_1$) or alternating dimerized/undimerized V–V chains ($M_2$/$M_3$), as shown in Figure 3D [57].

The degree of coupling between the electronic **Mott transition** and the structural transition (i.e., positioning on the Mott–Peierls spectrum) has been the subject of much controversy.

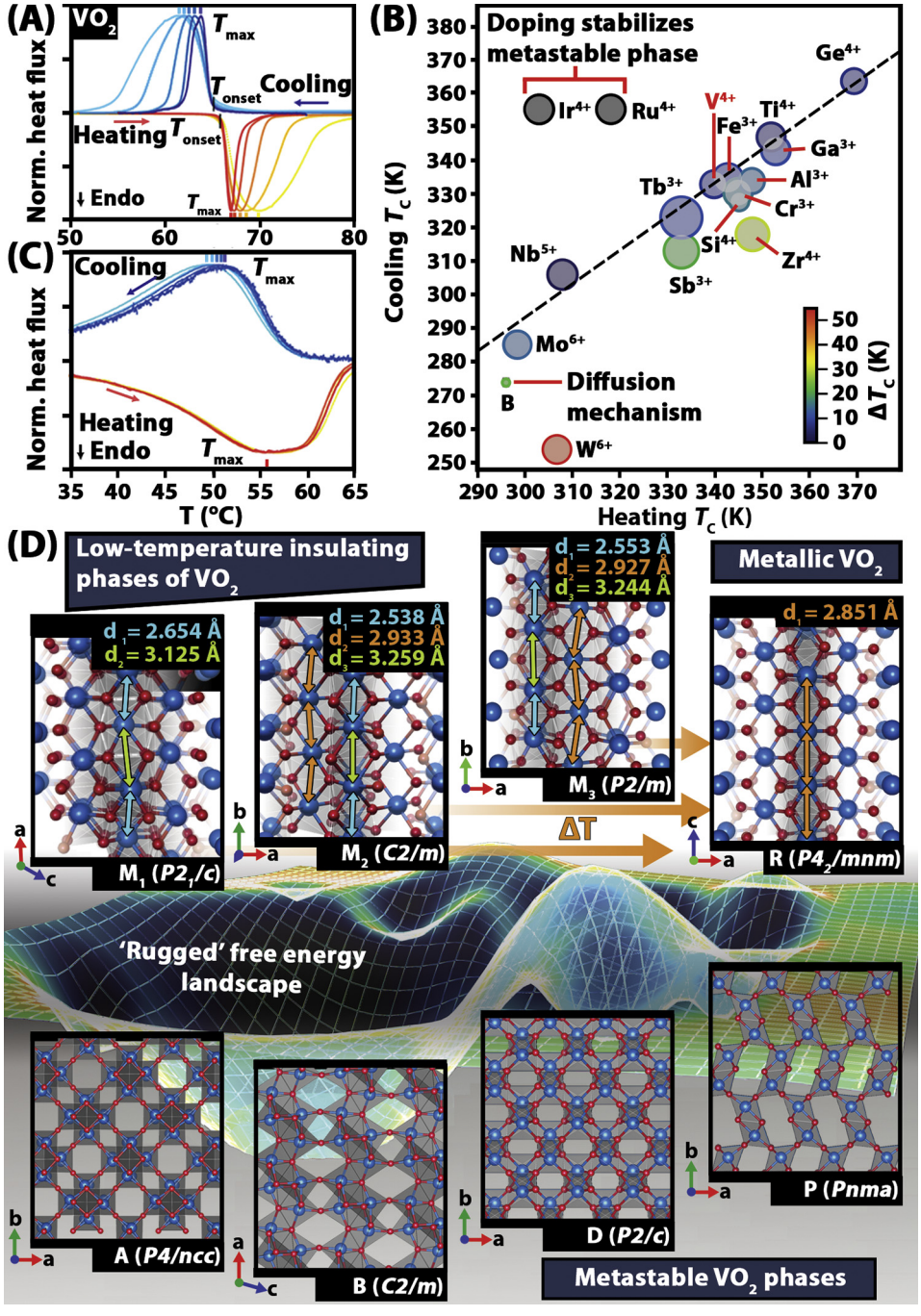


Figure 3. Metal–Insulator Transitions (MITs) in Vanadium Dioxide ($VO_2$). (A) Thermally induced MIT of $VO_2$ nanowires as measured by differential scanning calorimetry (DSC). The hysteresis becomes more pronounced with increasing ramp rate. (B) $VO_2$ can be doped with homovalent (e.g., $Ti^{4+}$) or aliovalent (e.g., $W^{6+}$) cations to alter the heating and cooling critical temperature ($T_C$) of the MIT. Reports of $T_C$ modulation on the incorporation of various dopants is summarized [19,56,61–67,70]. Effort was made to obtain data only from DSC (powders) or electrical resistivity measurements (thin films) and they were limited to studies providing diffraction data verifying retention of the $M_1/M_2$- (insulating) to-R (metallic)

*(Figure legend continued at the bottom of the next page.)*

Density functional theory (DFT) + dynamical mean-field theory (DMFT) calculations show that the MIT is impacted by correlation-driven effects that dictate intradimer exchange [39,58]. A recent neutron-scattering study provides a more quantitative accounting and suggests that phonons account for approximately two-thirds of the total increase in entropy at the MIT [59].

### Approaches to Modifying the MIT Threshold in $VO_2$

Two aspects of $VO_2$ are particularly relevant to its use as a **memristor** in neuromorphic computing applications: the transition temperature, $T_C$, and the thermal hysteresis width ($\Delta T_C = T_{Cooling} - T_{Heating}$). Deterministic control over $\Delta T_C$ is particularly important since a smaller hysteresis is required to minimize energy dissipation and achieve fast dynamics, whereas a large hysteresis could enable nonvolatile on/off states [19,60]. Importantly, $\Delta T_C$ in $VO_2$ is critically dependent on both intrinsic (doping, point defect concentration, and grain size; Figure 3B) [19,56,61–67] and extrinsic (strain) considerations [68,69].

The influence of incorporating a range of dopants in $VO_2$ at vanadium sites, at oxygen sites, or in tetrahedral holes has been investigated (Figure 3B) [19,56,61–67,70]. The inclusion of dopant atoms modifies the 'rugged' free-energy landscape of $VO_2$ (Figure 3D) in terms of relative phase stabilities and transformation barriers thereby nontrivially altering the coupling of lattice/electronic/spin degrees of freedom. As an example, tungsten strongly depresses the MIT and broadens the hysteresis [19,67,71]. In undoped $VO_2$, the thermal hysteresis is rate dependent and symmetric for both monoclinic➔rutile and rutile➔monoclinic transitions since the transitions appear to be nucleated at point defects (Figure 3A). On tungsten doping, $VO_2$ exhibits an asymmetric modulation of transition temperatures and dynamics (Figure 3C) [19,71]. Doping with tungsten [72] induces anisotropic lattice expansion and a local increase in symmetry around the dopant site [73], stabilizing $M_2$ domains (Figure 3D). The insulator➔metal transition in W-doped $VO_2$ is therefore facile, being nucleated at twin planes and $M_1/M_2$ stacking faults (wherein transformation dislocations can readily be stabilized) [29], whereas the reverse MIT originates at point defects such as oxygen vacancies that are suppressed on aliovalent tungsten doping. Tungsten doping thus functions similarly to tensile strain by enabling facile nucleation of rutile domains during the monoclinic➔rutile transformation but renders the reverse rutile➔monoclinic transformation more difficult, thereby engendering anisotropic hysteresis [72].

Alternatively, homovalent titanium doping raises the transition temperature and diminishes hysteresis width [74], which has been ascribed to the role of the dopant atoms in modifying the local lattice symmetry to mitigate lattice mismatch between the monoclinic and tetragonal polymorphs [63]. Germanium doping strongly increases the transition temperature, almost to 400 K (Figure 3B), which has been rationalized based on chemical pressure arguments, albeit that the local structure around the dopant Ge atom and its impact on the electronic structure of $VO_2$ remains to be elucidated [62]. Doping at the oxygen sites with fluorine or sulfur atoms is less explored and while modestly altering $T_C$ appears to degrade the magnitude of the transition [75]. An intriguing report illustrates nearly complete elimination of hysteresis on simultaneous incorporation of $Cr^{3+}$ and $Nb^{5+}$ in $VO_2$ [64]. In still other examples, dopants (e.g., $H^+$, $Ir^{4+}$, $Ru^{4+}$) [56,64,76]

transition. The broken line acts as a reference indicating symmetric change in the heating/cooling hysteresis ($\Delta T_C$) relative to undoped $VO_2$. The size and color of individual data points correspond to the crystal radius and the magnitude of hysteresis for each dopant, respectively. $T_C$ values have been selected based on the maximum solubility reported for a given dopant. Several dopants ($H^+$, $Ir^{4+}$, $Ru^{4+}$) stabilize insulating metastable polymorphs that do not transition to the metallic rutile phase [56,76]. (C) The intrinsic MIT properties of $VO_2$ can be modulated through dopant incorporation, which alters the relative thermodynamic stabilities and electronic structure of the insulating $M_1$ and metallic R phases. Tungsten doping has been shown to significantly lower the $T_C$ of $VO_2$ and alter the hysteresis width. (D) Structural relationships between the various reported polymorphs of $VO_2$ are shown. (A,C) adapted from [19]. Data in (B) collated from [19,56,61–67,70]. Structures in (D) collated from [56,116–118].

stabilize altogether different polymorphs (Figure 3D). Finally, interstitial doping of elemental boron into tetrahedral holes of the $M_1$ phase of $VO_2$ has recently been demonstrated, providing a notable post-synthetic approach to tuning $T_C$ and hysteresis of $VO_2$ [66]. Clear-cut design principles relating dopants to the transition temperature and hysteresis of $VO_2$ remain to be gleaned and will be pivotal to the utilization of $VO_2$ in neuromorphic computing.

### $NbO_2$: An Unusual High-Temperature MIT Material

$NbO_2$ (Figure 4Ai) also exhibits a pronounced MIT, albeit at a much higher temperature in the range 1000–1100 K [15,77]. Despite striking similarities to $VO_2$, a mechanistic understanding of the underlying MIT has emerged only recently [54,78,79]. On heating, $NbO_2$ transitions from a distorted rutile structure with dimerized Nb–Nb pairs (2.685 Å and 3.304 Å; Figure 4Ai,ii) to a high-symmetry rutile structure with uniform Nb–Nb distances (3.032 Å; Figure 4Aiii,iv) [77,79]. Thus, the low-temperature Nb–Nb dimers are decoupled across this phase transition (Figure 4A), resulting in quasilinear Nb chains and manifesting an order-of-magnitude spike in conductivity [15,54,79,80]. Electron correlation is expected to play a less-significant role in $NbO_2$ compared with $VO_2$ owing to the greater energy dispersion of 4d bands; Demkov has noted the emergence of soft phonon modes in the Brillouin zone, a hallmark of the Peierls instability [79]. Even so, a comparative DFT+DMFT investigation has demonstrated that electronic correlations, although less prominent, are non-negligible [54]. This is supported by observations of strong renormalization of the $t_{2g}$ levels, concurrent with the emergence of Hubbard sub-bands in the metallic phases of both $VO_2$ and $NbO_2$ [54].

Given the strong parallels between $NbO_2$ and $VO_2$, attempts to alloy $VO_2$ and $NbO_2$ to achieve a $T_C$ intermediate between the two seems a straightforward solution. Doping $NbO_2$ with 5 at.% V results in a ~100-K decrease in $T_C$. However, the lattice incongruence, coupled with the large discrepancy in ionic radii, leads to the stabilization of a semiconducting phase (for $0.95 > x > 0.05$ in $Nb_{1-x}V_xO_2$), which does not undergo an MIT [77].

### Leveraging the MIT in $NbO_2$ to Realize Brain-like Computing

Recent results for $NbO_2$ have highlighted its viability as a neuromorphic material [14,15,79,81], emphasizing the importance of **'negative differential resistance' (NDR)** (defined as $dV/dI < 0$) behavior as a hallmark of memristive properties (Figure 1D) [24,26,82]. Unlike traditional circuit elements, voltage-driven memristors are nonlinear dynamical elements for which current ($I$) evolves with time ($t$) as

$$I(t) = G(\Theta, V)V(t) \quad [1]$$

and

$$d\Theta/dt = f(\Theta, V), \quad [2]$$

where $V$ is the time-dependent input voltage and $G$ is the conductance, which is a function of $V$ and an internal state variable $\Theta$ (in this case temperature). The rate of change of the state variable depends on the value of the state variable (thus incorporating memory) and $V$ [6,14,83].

Two distinct NDR regimes are observed in $NbO_2$ (Figure 1D) and are driven by nonlinear thermally activated conduction and the MIT, potentially allowing decoupling of the nonlinear conductance response from the atomic rearrangement. This, combined with the demonstration of 'edge of chaos' dynamics reminiscent of neuronal function [14], has generated much interest in $NbO_2$ as a neuromorphic computing material; however, the high transition temperature of $NbO_2$ (1050–1100 K) [15,77,80] and the dominance of the Peierls-type transition results in excessive

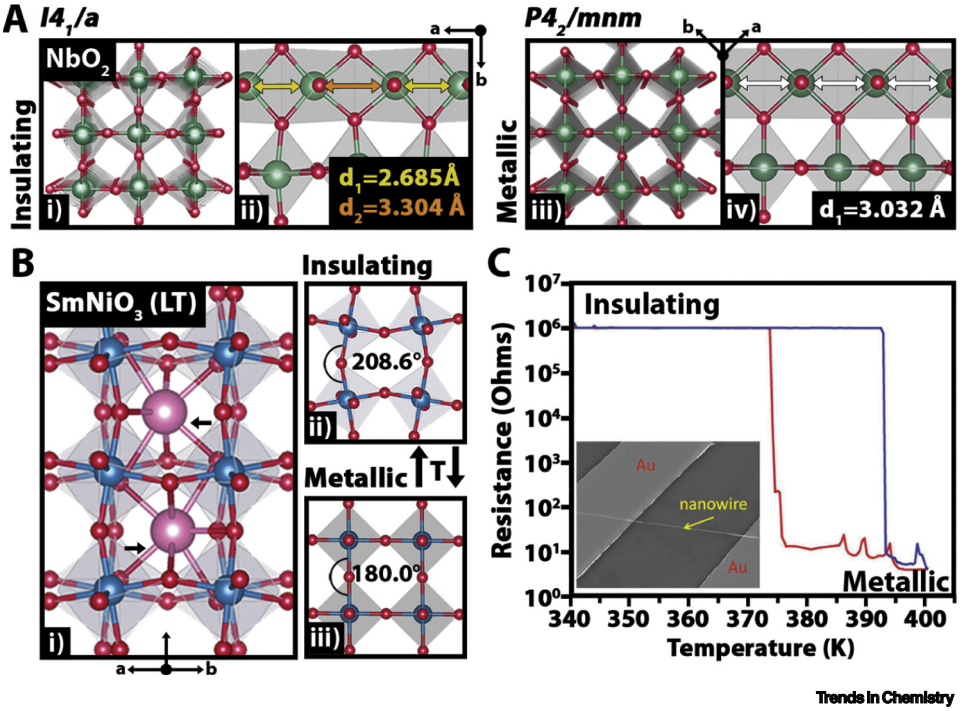


Figure 4. Metal–Insulator Transitions (MITs) in Niobium Dioxide ($NbO_2$), $RENiO_3$, and $M_xV_2O_5$. (A) The MIT of $NbO_2$ is underpinned by a phase transition between low- and high-symmetry tetragonal distortions. The low-temperature ($I4_1/a$) phase of $NbO_2$ exhibits distinct Nb–Nb dimers (alternating 2.685- and 3.304-Å distances), whereas the high-temperature phase ($P4_2/mnm$) exhibits a singular Nb–Nb distance (3.032 Å). As discussed in the text, the structural transition plays a considerably greater role in the MIT of $NbO_2$ compared with vanadium dioxide ($VO_2$). (B) A simplified representation of structural perturbations observed in samarium nickelate ($SmNiO_3$) across its MIT, showing only an exaggerated change in the <O–Ni–O> bond angle across the MIT. Breathing distortions comprising alternating $NiO_6$ octahedra are omitted. (C) As an exemplar of the electronic instabilities of $M_xV_2O_5$ phases, the MIT in β/β′-$Cu_xV_2O_5$ is observed to occur with retention of the 1D tunnel framework [23,115]. (C) adapted from [23].

energy consumption. By comparison, $VO_2$ consumes just 16% of the energy per switch and can be switched 100× times faster than $NbO_2$ [6,14]. This is succinctly reflected in their respective volumetric free-energy cost to trigger an MIT (<1 fJ·spike$^{-1}$ for $VO_2$ and ~6 fJ·spike$^{-1}$ for $NbO_2$) [6,84]. Despite promising results for $VO_2$, its $T_C$ (~340 K) is low, reinforcing the importance of understanding the mechanisms by which Ti, Ga, and Ge doping increase $T_C$ and the identification of methods that allow amplification of this effect [62,63,74]. In light of energy-efficiency considerations, subsequent sections emphasize the design and stabilization of materials with greater electronic (rather than lattice) contributions.

## Towards an Expanded Palette: Rare-Earth Nickelates and Mixed-Valence Vanadium Oxides as Neuromorphic Materials

### Perovskites Take the Stage with Rare-Earth Nickelates

Rare-earth nickelates and ternary vanadium oxides provide a vastly expanded design space enabled by ternary and quaternary compositions, thereby expanding the scope for tuning electronic instabilities and thus transition temperatures [16,30,85,86]. Rare-earth nickelates ($RENiO_3$) belong to a family of oxide perovskites that adopt distortions from a nominally cubic ($Pm\bar{3}m$) structure [25,48,87]. With the exception of $LaNiO_3$ which is always metallic [87], $RENiO_3$ (RE = Pr, Nd, Sm, Eu, Gd, Dy, Ho, Er, Lu) compounds exhibit a sharp MIT that can be tuned across a wide range ($T_C$ = 130–599 K; Figure 2E) [25,30,88,89]. Strain in cubic perovskite structures can be

applied 'chemically' by varying the size of the rare-earth cation [48,90,91] or extrinsically by epitaxial mismatch [25,92–94]. Analogous to $VO_2$ and $NbO_2$, the MIT of $RENiO_3$ is concomitant with a structural transition distinguished by a loss of symmetry from orthorhombic (*Pbnm*) in the metallic state to monoclinic ($P2_1/n$) in the insulating state [48,90,95–98]. Locally, the MIT is observed to coincide with a slight 'breathing' distortion that involves the concerted motion of nickel-centered octahedra, inevitably altering Ni 3d–O 2p hybridization [99] and stabilizing chains of alternating inequivalent Ni polyhedra with long and short Ni–O bonds [41,100,101]. An early proposed mechanism for the resistance-switching phenomenon invoked a charge disproportionation mechanism, wherein the 'breathing' lattice distortion was accompanied by disproportionation to a mixed Ni valence state [i.e., $2(d^7) \rightarrow d^{7+\delta} + d^{7-\delta}$] [91,97,100]. However, a definitive mechanism for the MIT in $RENiO_3$ has been difficult to ascertain.

Recent consensus delineates $RENiO_3$ materials as **'negative-charge-transfer' insulators** (Figure 2C) whereby hybridization between occupied O 2p and unoccupied Ni 3d states give rise to a p/d–p/d quasigap [30,41,42,102]. Resonant inelastic X-ray scattering (RIXS) supported by many-body cluster and single-impurity Anderson model (SIAM) calculations point to a negative-charge-transfer scenario as the underlying electronic origin of the observed conductance modulation (Figure 2C) [41,42,102]. Interestingly, Bisogni and colleagues [41] have proposed the emergence of an O 2p–O 2p quasigap owing to an increased number of holes in the O 2p band, which deviates somewhat from the explicit hybridization of overlapping O 2p–Ni 3d states invoked in other studies [30,103,104]. In the insulating state, the migration of a Ni hole to hybridized oxygen 2p states is observed [41]. Another model suggests that a pair of ligand holes ($L^2$) strongly couples with the breathing-type lattice distortion by occupying alternating $NiO_6$ octahedra (bipolaron condensation) [101]. In this mechanism, Ni 3d electrons on one sublattice ($3d^8$) are decoupled from nearby octahedra undergoing the observed stretching motion ($3d^8L^2$) [105]. Each adjacent sublattice then distorts along specific phonon modes to maximize delocalization of the holes between the O 2p and Ni 3d states. The so-called 'site-selective Mott transition' mechanism has gained recent experimental support [41,102]. While the precise underlying mechanisms remain to be elucidated, these compounds illustrate a distinctive mode of coupling of electronic structure (negative charge transfer, charge disproportionation, site-selective Mott transitions) with lattice distortions (breathing distortions and octahedral rotations) corroborating the idea of a mechanistic spectrum spanning structural and electronic considerations coupled to different degrees [92,100–102].

The extent of perturbation of bond angles required to close the negative charge-transfer gap is in essence correlated with the Goldschmidt tolerance factors [48] of the perovskite structure and thus smoothly varies across the lanthanide series. Thus, $T_C$ can be varied systematically either through chemical substitution at the rare-earth site or through epitaxial strain [89,92,93]. Despite the smooth variation of the MIT temperature across the lanthanide series and the generally high miscibility of lanthanides, the formation of solid solutions remains underexplored. Huang and coworkers have demonstrated the use of Sm and Nd miscibility to bridge the gap between the MITs of samarium nickelate ($SmNiO_3$) and $NdNiO_3$ [91]. Superlattices and random alloying on both rare-earth and nickel lattices warrant further exploration to establish independent control of transformation characteristics [91].

Alternatively, lattice mismatch by epitaxial growth of $RENiO_3$ thin films on different substrates provides a tool for tuning $T_C$ and has been extensively explored for $SmNiO_3$ (Figure 4B). At relatively modest strains, a large diminution of $T_C$ is observed, from 380 K to 140 K. Inducing a strain of $\varepsilon = -2.3\%$ by epitaxial growth on a yttrium orthoaluminate ($YAlO_3$) substrate completely suppresses the insulating phase within the measured temperature range ($T > 4$ K) [25,93]. While evidently powerful, modulation of the conductance response by epitaxial strain renders $T_C$ static and the

use of epitaxial strain to increase $T_C$ has not been demonstrated. By contrast, ionic liquid gating provides a means of dynamically modulating $T_C$ [20,94,106]. Nickelates can reversibly accommodate large concentrations of oxygen vacancies [88,91]. Ramanathan has demonstrated that the creation of oxygen vacancies through ionic-liquid-induced gating affords deterministic control of the conductivity of $SmNiO_3$ transistors on the application of a gate voltage, thereby yielding a means of mimicking synaptic function with time-correlated spikes [20]. Despite much work devoted to tuning $T_C$ in $RENiO_3$, little attention has been devoted to tuning hysteresis.

## Ternary Vanadium Oxides as a Promising Design Space

Ternary vanadium oxides ($M_xV_2O_5$) crystallize in a variety of low-dimensional motifs including quasi-1D tunnels (Figure 5) and quasi-2D layered structures with varying stacking sequences and extents of condensation (single/double layered) [16,21,23,24,107]. $M_xV_2O_5$ are nominally mixed valence in the ground state; they are formed by the reductive intercalation of various cations that span the breadth of the periodic table (s-block, transition metal, p-block; Figure 5) as well as organic cations in different frameworks of $V_2O_5$ [21–23,107–111]. The rugged energy landscape of $V_2O_5$ is characterized by scores of possible metastable structures; upwards of six have been experimentally stabilized [28,86,109,112]. On intercalation, the $V_2O_5$ lattice is partially reduced, resulting in a mixture of $V^{4+}/V^{5+}$ oxidation states. Given the strong degree of electron correlation in V 3d bands, electrons tend to localize on vanadium sites adjacent to intercalating cations, forming charge-ordered patterns characterized by the formation of **Mott–Hubbard bands** rather than delocalized metals (Figure 1B) [113]. Many of these materials undergo a Mott MIT with only a slight structural contribution derived from ionic rearrangement of the intercalated cations or pinching of the $V_2O_5$ framework [21–23,107]. With increasing temperature, select bond distances are decreased, leading to increased electronic coupling between adjacent metal centers (Figure 2B). Thus, the MIT is critically dependent on V–V distances within the structure, the carrier density, and the positioning of intercalated-ion-derived 'midgap' states [85,107,108,114]. This is evidenced in the $M_xV_2O_5$ series for (M = alkali metals) wherein the transition temperature ($T_C$) monotonically increases with decreasing ionic radius (for similar values of $x$), which is correlated with the V–V bond distance along the $b$-axis [111]. The wealth of electronic phase transitions in $M_xV_2O_5$ systems has been widely demonstrated in the form of MIT [22,23,49,107,111,114,115] and semiconductor–semiconductor transitions [21] facilitated by Mott instabilities.

In contrast to the previous systems, the spin, orbital, and electronic degrees of freedom in $M_xV_2O_5$ compounds are to a greater extent independently tunable through selection of the intercalated cation (M) [21–23,49,107], its stoichiometry ($x$), and the vanadium–oxygen connectivity of the polymorph (single/double-layered, quasi-1D, etc.). The frameworks are furthermore characterized by distinctive interstitial sites that can accommodate specific cations, enabling stabilization of quaternary compositions with ordered arrays of different intercalated cations. Topochemical methods have been developed to extract 'native' cations, to stabilize metastable $V_2O_5$ polymorphs [28,86], and to insert altogether different ions to access compounds inaccessible from direct synthesis (Figure 5). β-$M_xV_2O_5$ (M = Mg, Sn, Co, Ni) [108,109] have been prepared by this route; p-block cations with stereoactive lone-pair electrons introduce a midgap state within the bandgap rendering these compounds amenable to voltage-induced MITs [107,114]. Recently, massive MITs have been observed for individual single-crystalline nanowires (Figure 4C) [21,22,49], albeit that the sensitivity to stoichiometry, $x$, makes it difficult to fully unravel the coupling of electronic structure and lattice distortions. One proposed mechanism suggests bandwidth broadening owing to anharmonic copper oscillations [23,115]. In the case of δ-$Ag_xV_2O_5$, high-resolution X-ray diffraction has been used to evaluate the structure above and below the MIT. Subtle changes in the V–V distance indicate increased V $d_{xy}$ overlap as the origin of the MIT, consistent with an increase in the bandwidth of the LH band bridging the Mott gap [21].

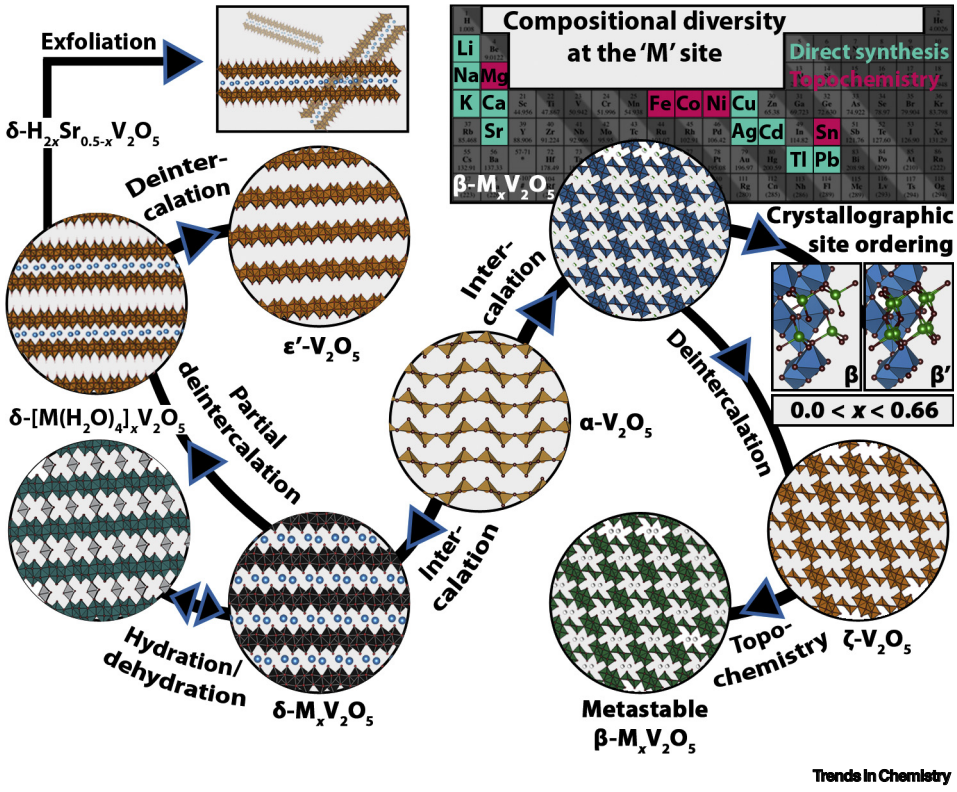


Figure 5. Intercalation-Induced Transformations in the $M_xV_2O_5$ Phase Space. Thermodynamically stable single-layered α-$V_2O_5$ (center) can be intercalated with alkali metals (Li, Na, K), alkaline metals (Mg, Ca, Sr), transition metals (Co, Ni, Cu, Zn, Ag), and p-block elements (Sn, Pb, Tl) to form ternary vanadium oxides ($M_xV_2O_5$) with substantially altered vanadium–oxygen frameworks. Depending on the size of the intercalating ion, M, and its stoichiometry, *x*, the framework rearranges to form 'double-layered' (left) or tunnel-structured (right) phases. Soft chemistry can be utilized to induce transformations that allow control over the extent of electronic coupling between adjacent vanadium metal centers. The layered δ-$M_xV_2O_5$ structures can be reversibly hydrated to form hydrated materials, δ-$[M(H_2O)_4]_xV_2O_5$, that have been shown to exhibit pinched *I*/*V* hysteresis loops characteristic of memristors. These materials can be partially leached and exfoliated to alter the extent of electronic coupling between adjacent $V_4O_{10}$ double layers or fully leached to form a metastable $V_2O_5$ polymorph [86,110,112]. Alternatively, tunnel-structured β-$M_xV_2O_5$ phases can be stabilized (right) for several intercalants (light blue, Periodic Table) [21,107]. Topochemical modification enables control over the stoichiometry, *x*, and the crystallographic site (β/β′) occupied by the metal cation and therefore the extent of charge ordering. The intercalated ions can be completely leached to stabilize a new metastable polymorph, ζ-$V_2O_5$, that exhibits significantly different V–O hybridization compared with the thermodynamically stable α-$V_2O_5$ phase [109]. This empty polymorph can finally be re-intercalated with additional metals to form metastable ternary vanadium oxides (pink, Periodic Table), representing a method for installing specific electronic states [108,109]. Structures in (E) based on original data reported in [23,24,108–110,112].

Exfoliation of these layered quasi-2D $M_xV_2O_5$ materials has been explored and provides an additional knob for tuning electron correlation and bandgap by alteration of local symmetry [110,112]. The intercalated ions in such 2D systems can further be solvated to form materials with the composition δ-$[M(H_2O)_4]_xV_2O_5$ (M = Co, Ni, Zn), which have furthermore been shown to exhibit memristive behavior ascribed tentatively to proton diffusion [24]. The insertion of solvated ions further suggests that the discipline of coordination chemistry has much to contribute to controlling electron delocalization on the $V_2O_5$ framework.

## Concluding Remarks

Recently, using only two $VO_2$ memristors, Yi and colleagues were able to simulate 23 distinct biological neuron spiking behaviors. By contrast, a CMOS artificial neuron made from 1300

## Outstanding Questions

While considerable recent attention has focused on the use of AI to accelerate the design of novel materials, can novel neuromorphic materials accelerate the realization of the promise of AI?

How can fundamental descriptors of transformation characteristics be formulated in terms of intrinsic materials properties, mesoscale domain evolution, and the interaction of defects and domains with external fields?

How can transformation characteristics such as magnitude of conductance switching, threshold energy, heat dissipation, switching time, hysteresis, dynamics of relaxation, and number of accessible internal states be decoupled from each other and independently modulated?

Can the critical transition temperature of $VO_2$ be pushed above 400 K by amplifying the influence of specific dopants and coupling to external fields?

How can codoping schemes be developed to amplify or decouple transformation characteristics?

Can diffusive interstitial dopants introduced in close-packed structures be used to obtain strongly time-variant responses of the metal–insulator transition? Can electronic structure measurements of $M_xV_2O_5$ compounds performed as a function of composition (M), stoichiometry (*x*), and framework connectivity be used to benchmark and improve the theoretical treatment of electron correlation?

How best can the vast design space of $M_xV_2O_5$ compounds spanning composition, stoichiometry, and diverse crystallographic sites be navigated to arrive at compounds with the desired transformation characteristics?

Can solid solutions of $RENiO_3$ (e.g., $Nd_{0.5}Sm_{0.5}$, $Y_{0.3}Sm_{0.7}$) be stabilized across the entire phase space to tailor transition temperatures deterministically between the end members?

What intrinsic and extrinsic factors control hysteresis width and switching magnitudes in rare-earth nickelates?

What is the mechanistic basis for the classical memristive behavior observed for δ-$[M(H_2O)_4]_xV_2O_5$ compounds?

Can machine learning methods enable accelerated evaluation of free-energy landscapes in search of proximate wells with tunable transformation barriers that can be utilized as neuromorphic vectors?

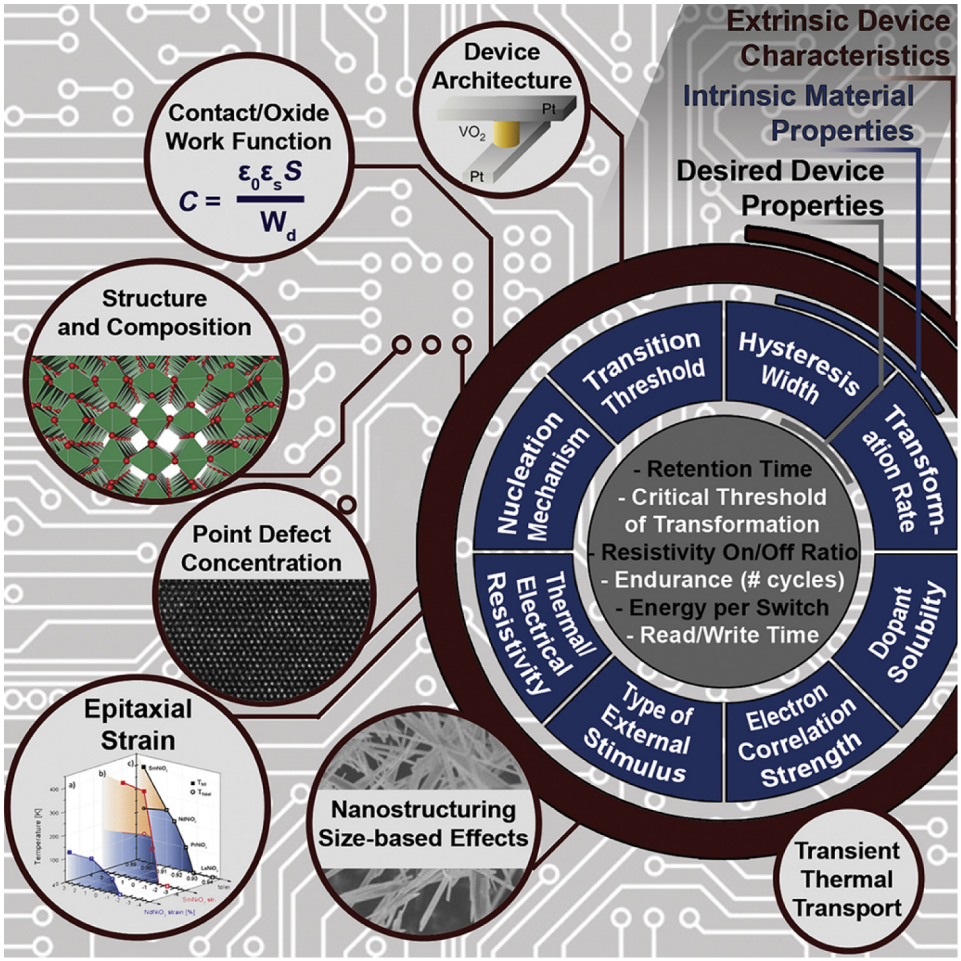


Figure 6. The Coupling of Intrinsic Chemical Properties and Extrinsic Characteristics in Determining Neuromorphic Function. Schematic delineating desired device characteristics (gray inner circle), tunable intrinsic material properties derived from composition and structure (blue circle), and tunable extrinsic device/materials characteristics (maroon circle, exterior circles). Images in maroon 'Extrinsic device characteristics' circles adapted in part from [6,19,24,25].

logic gates was able to simulate only 11 neuronal behaviors [6]. The realization of the full promise of neuromorphic computing requires the design of new dynamical materials and systems that directly emulate the functionality of neurons and synapses to weave memory, computation, and communication into one fabric. Rather than build 'better transistors', we need to develop novel dynamical materials with nonlinear conductance switching that directly emulate neuronal elements and to build entirely new circuit elements from such materials that can perform tasks that presently require hundreds to thousands of transistors. Such an advance will increase the energy efficiency of computing by orders of magnitude; this is furthermore required since most computation will need to be performed at 'the edge of the internet', in close proximity to where data are collected and where power availability is likely to be low and intermittent. Such high-fidelity neuronal emulation at 'the edge' will enable immediate system updating (learning) in response to external events, thereby enabling realization of the full promise of artificial intelligence (AI) to learn and respond in real time.

While considerable recent attention has focused on the use of AI to accelerate the design of novel materials and syntheses, novel compounds and syntheses are urgently needed to allow realization of the promise of AI in full measure. The design of materials that 'turn on a dime' requires the elucidation of design principles underpinning electronic instabilities as well as independent control of transformation characteristics such as the transition temperature, hysteresis width, magnitude of conductance switching, dynamics of relaxation between states, and number of accessible internal states (Figure 6). Deterministic control of conduction pathways is further an urgent imperative. The interplay between device properties, intrinsic chemical descriptors, and extrinsic tunable properties is illustrated in Figure 6. Please see the Outstanding Questions for a succinct summary of fundamental chemistry questions that must be addressed, practical challenges that must be met, and a summary of several promising and emerging directions that will play a role in addressing these issues. The challenges described here span the discovery of new compounds, synthetic approaches to stabilizing metastable compounds to obtain independent control of transformation characteristics, and the understanding of dynamical processes away from equilibrium, which represents a rich new frontier at the intersection of chemistry and information science.

## Acknowledgments

S.B., J.L.A., and D.A.S. acknowledge partial support from the National Science Foundation under NSF grant DMR 1809866. The research was funded in part by award # A-1978-20190330 from the Welch Foundation. J.L.A. acknowledges support from a NASA Space Technology Research Fellowship under grant number 80NSSC17K0182.

## References

1. Schuller, I.K. and Stevens, R. (2015) *Neuromorphic Computing: From Materials to Systems Architecture – Report of a Roundtable Convened to Consider Neuromorphic Computing Basic Research Needs*, US Department of Energy
2. Salahuddin, S. *et al.* (2018) The era of hyper-scaling in electronics. *Nat. Electron.* 1, 442–450
3. Taylor, M.B. (2013) A landscape of the new dark silicon design regime. *IEEE Micro.* 33, 8–19
4. Ionescu, A.M. and Riel, H. (2011) Tunnel field-effect transistors as energy-efficient electronic switches. *Nature* 479, 329–337
5. Yang, C.S. *et al.* (2017) A synaptic transistor based on quasi-2D molybdenum oxide. *Adv. Mater.* 29, 1700906
6. Yi, W. *et al.* (2018) Biological plausibility and stochasticity in scalable $VO_2$ active memristor neurons. *Nat. Commun.* 9, 4661
7. Hodgkin, A.L. and Huxley, A.F. (1939) Action potentials recorded from inside a nerve fibre. *Nature* 144, 710–711
8. Torrejon, J. *et al.* (2017) Neuromorphic computing with nanoscale spintronic oscillators. *Nature* 547, 428–431
9. Crane, H. (1962) Neuristor-a novel device and system concept. *Proc. IRE* 50, 2048–2060
10. Jouppi, N.P. *et al.* (2017) In-datacenter performance analysis of a tensor processing unit. In *Proceedings of the 44th Annual International Symposium on Computer Architecture*, ISCA
11. Merolla, P.A. *et al.* (2014) A million spiking-neuron integrated circuit with a scalable communication network and interface. *Science* 345, 668–673
12. Stoliar, P. *et al.* (2017) A leaky-integrate-and-fire neuron analog realized with a Mott insulator. *Adv. Funct. Mater.* 27, 1604740
13. Han, J.W. and Meyyappan, M. (2018) Leaky integrate-and-fire biristor neuron. *IEEE Electron. Device Lett.* 39, 1457–1460
14. Kumar, S. *et al.* (2017) Chaotic dynamics in nanoscale $NbO_2$ Mott memristors for analogue computing. *Nature* 548, 318–321
15. Kumar, S. *et al.* (2017) Physical origins of current and temperature controlled negative differential resistances in $NbO_2$. *Nat. Commun.* 8, 658
16. Marley, P.M. *et al.* (2015) Transformers: the changing phases of low-dimensional vanadium oxide bronzes. *Chem. Commun.* 51, 5181–5198
17. Wang, Z. *et al.* (2017) Memristors with diffusive dynamics as synaptic emulators for neuromorphic computing. *Nat. Mater.* 16, 101–108
18. Wang, Z. *et al.* (2018) Capacitive neural network with neuro-transistors. *Nat. Commun.* 9, 3208
19. Braham, E.J. *et al.* (2018) Modulating the hysteresis of an electronic transition: launching alternative transformation pathways in the metal–insulator transition of vanadium(IV) oxide. *Chem. Mater.* 30, 214–224
20. Shi, J. *et al.* (2013) A correlated nickelate synaptic transistor. *Nat. Commun.* 4, 3676
21. Marley, P.M. *et al.* (2014) Electronic phase transitions of δ-$Ag_xV_2O_5$ nanowires: interplay between geometric and electronic structures. *J. Phys. Chem. C* 118, 21235–21243
22. Patridge, C.J. *et al.* (2010) Synthesis, spectroscopic characterization, and observation of massive metal–insulator transitions in nanowires of a nonstoichiometric vanadium oxide bronze. *Nano Lett.* 10, 2448–2453
23. Patridge, C.J. *et al.* (2011) Colossal above-room-temperature metal–insulator switching of a Wadsley-type tunnel bronze. *Chem. Commun.* 47, 4484–4486
24. Andrews, J.L. *et al.* (2017) Memristive response of a new class of hydrated vanadium oxide intercalation compounds. *MRS Commun.* 7, 634–641
25. Catalano, S. *et al.* (2014) Electronic transitions in strained $SmNiO_3$ thin films. *APL Mater.* 2, 116110
26. Pickett, M.D. *et al.* (2012) A scalable neuristor built with Mott memristors. *Nat. Mater.* 12, 114–117
27. Li, S. *et al.* (2018) Anatomy of filamentary threshold switching in amorphous niobium oxide. *Nanotechnology* 29, 375705
28. Parija, A. *et al.* (2018) Traversing energy landscapes away from equilibrium: strategies for accessing and utilizing metastable phase space. *J. Phys. Chem. C* 122, 25709–25728
29. Hudak, B.M. *et al.* (2017) Real-time atomistic observation of structural phase transformations in individual hafnia nanorods. *Nat. Commun.* 8, 15316
30. Middey, S. *et al.* (2016) Physics of ultrathin films and heterostructures of rare-earth nickelates. *Annu. Rev. Mater. Res.* 46, 305–334
31. Goodenough, J.B. (1971) Metallic oxides. *Prog. Solid State Chem.* 5, 145–399
32. Fulde, P. *et al.* (2006) Strongly correlated electrons. *Solid State Phys.* 60, 1–180

33. Elbio, D. (2005) Complexity in strongly correlated electronic systems. *Science* 309, 257–262
34. Basov, D.N. *et al.* (2011) Electrodynamics of correlated electron materials. *Rev. Mod. Phys.* 83, 471–541
35. Imada, M. *et al.* (1998) Metal–insulator transitions. *Rev. Mod. Phys.* 70, 1039–1263
36. Monceau, P. (2012) Electronic crystals: an experimental overview. *Adv. Phys.* 61, 325–581
37. Wang, Z. *et al.* (2018) Threshold switching of Ag or Cu in dielectrics: materials, mechanism, and applications. *Adv. Funct. Mater.* 28, 1704862
38. Yang, D.-S. *et al.* (2016) Ultrafast electron crystallography of the cooperative reaction path in vanadium dioxide. *Struct. Dyn.* 3, 034304
39. Brito, W.H. *et al.* (2016) Metal–insulator transition in $VO_2$: a DFT + DMFT perspective. *Phys. Rev. Lett.* 117, 056402
40. Jeong, J. *et al.* (2013) Suppression of metal-insulator transition in $VO_2$ by electric field-induced oxygen vacancy formation. *Science* 339, 1402–1405
41. Bisogni, V. *et al.* (2016) Ground-state oxygen holes and the metal–insulator transition in the negative charge-transfer rare-earth nickelates. *Nat. Commun.* 7, 13017
42. Rogge, P.C. *et al.* (2018) Electronic structure of negative charge transfer $CaFeO_3$ across the metal-insulator transition. *Phys. Rev. Mater.* 2, 015002
43. Sun, K. *et al.* (2018) Hidden CDW states and insulator-to-metal transition after a pulsed femtosecond laser excitation in layered chalcogenide 1T-$TaS_{2-x}Se_x$. *Sci. Adv.* 4, 9660
44. Zhang, S. *et al.* (2019) A spin–orbit-torque memristive device. *Adv. Electron. Mater.* 5, 1800782
45. Chang, C.F. *et al.* (2018) *c*-Axis dimer and its electronic breakup: the insulator-to-metal transition in $Ti_2O_3$. *Phys. Rev. X* 8, 021004
46. Greenberg, E. *et al.* (2018) Pressure-induced site-selective Mott insulator–metal transition in $Fe_2O_3$. *Phys. Rev. X* 8, 031059
47. Bartholomew, R.F. and Frankel, D.R. (1969) Electrical properties of some titanium oxides. *Phys. Rev.* 187, 828–833
48. Torrance, J. *et al.* (1992) Systematic study of insulator-metal transitions in perovskites $RNiO_3$ (R=Pr,Nd,Sm,Eu) due to closing of charge-transfer gap. *Phys. Rev. B* 45, 8209–8212
49. Wu, T.-L. *et al.* (2012) Electrically driven metal-insulator switching in δ-$K_xV_2O_5$ nanowires. *Appl. Phys. Lett.* 101, 163502
50. Kachi, S. *et al.* (1973) Metal–insulator transition in $V_nO_{2n-1}$. *J. Solid State Chem.* 6, 258–270
51. Catalano, S. *et al.* (2018) Rare-earth nickelates $RNiO_3$: thin films and heterostructures. *Rep. Prog. Phys.* 81, 046501
52. Zhang, X. *et al.* (2011) Synthetic beta-$K_{0.33}V_2O_5$ nanorods: a metal–insulator transition in vanadium oxide bronze. *Chem. Asian J.* 6, 3230–3235
53. Tanaka, K. *et al.* (2015) Structural phase transition between γ-$Ti_3O_5$ and δ-$Ti_3O_5$ by breaking of a one-dimensionally conducting pathway. *Cryst. Growth Des.* 15, 653–657
54. Brito, W.H. *et al.* (2017) Dynamic electronic correlation effects in $NbO_2$ as compared to $VO_2$. *Phys. Rev. B* 96, 195102
55. Kumar, S. *et al.* (2014) Sequential electronic and structural transitions in $VO_2$ observed using X-ray absorption spectromicroscopy. *Adv. Mater.* 26, 7505–7509
56. Braham, E.J. *et al.* (2018) Stabilization of a metastable tunnel-structured orthorhombic phase of $VO_2$ upon iridium doping. *Phys. Status Solidi Appl. Mater. Sci.* 215, 1700884
57. Whittaker, L. *et al.* (2011) Microscopic and nanoscale perspective of the metal–insulator phase transitions of $VO_2$: some new twists to an old tale. *J. Phys. Chem. Lett.* 2, 745–758
58. Nájera, O. *et al.* (2017) Resolving the $VO_2$ controversy: Mott mechanism dominates the insulator-to-metal transition. *Phys. Rev. B* 95, 035113
59. Budai, J.D. *et al.* (2014) Metallization of vanadium dioxide driven by large phonon entropy. *Nature* 515, 535–539
60. Shank, J.C. *et al.* (2018) Scalable memdiodes exhibiting rectification and hysteresis for neuromorphic computing. *Sci. Rep.* 8, 12935
61. Krammer, A. *et al.* (2017) Study of Si doped $VO_2$ thin films for solar thermal applications. *Energy Procedia* 122, 745–750
62. Krammer, A. *et al.* (2017) Elevated transition temperature in Ge doped $VO_2$ thin films. *J. Appl. Phys.* 122, 045304
63. Wu, Y. *et al.* (2015) Decoupling the lattice distortion and charge doping effects on the phase transition behavior of $VO_2$ by titanium ($Ti^{4+}$) doping. *Sci. Rep.* 5, 9328
64. Miyazaki, K. *et al.* (2016) Chromium–niobium co-doped vanadium dioxide films: large temperature coefficient of resistance and practically no thermal hysteresis of the metal–insulator transition. *AIP Adv.* 6, 055012
65. Wang, N. *et al.* (2016) Terbium-doped $VO_2$ thin films: reduced phase transition temperature and largely enhanced luminous transmittance. *Langmuir* 32, 759–764
66. Alivio, T.E.G.G. *et al.* (2017) Postsynthetic route for modifying the metal–insulator transition of $VO_2$ by interstitial dopant incorporation. *Chem. Mater.* 29, 5401–5412
67. Patridge, C.J. *et al.* (2012) Elucidating the influence of local structure perturbations on the metal–insulator transitions of $V_{1-x}Mo_xO_2$ nanowires: mechanistic insights from an X-ray absorption spectroscopy study. *J. Phys. Chem. C* 116, 3728–3736
68. Park, J.H. *et al.* (2013) Measurement of a solid-state triple point at the metal–insulator transition in $VO_2$. *Nature* 500, 431–434
69. Fan, W. *et al.* (2011) Large kinetic asymmetry in the metal–insulator transition nucleated at localized and extended defects. *Phys. Rev. B* 83, 235102
70. Wu, Y. *et al.* (2014) A novel route to realize controllable phases in an aluminum ($Al^{3+}$)-doped $VO_2$ system and the metal–insulator transition modulation. *Mater. Lett.* 127, 44–47
71. Whittaker, L. *et al.* (2011) Distinctive finite size effects on the phase diagram and metal–insulator transitions of tungsten-doped vanadium(IV) oxide. *J. Mater. Chem.* 21, 5580–5592
72. Yang, M. *et al.* (2016) Suppression of structural phase transition in $VO_2$ by epitaxial strain in vicinity of metal–insulator transition. *Sci. Rep.* 6, 23119
73. Asayesh-Ardakani, H. *et al.* (2015) Atomic origins of monoclinic-tetragonal (rutile) phase transition in doped $VO_2$ nanowires. *Nano Lett.* 15, 7179–7188
74. Chen, S. *et al.* (2014) Unraveling mechanism on reducing thermal hysteresis width of $VO_2$ by Ti doping: a joint experimental and theoretical study. *J. Phys. Chem. C* 118, 18938–18944
75. Riapanitra, A. *et al.* (2018) Supercritical temperature synthesis of fluorine-doped $VO_2$(M) nanoparticle with improved thermochromic property. *Nanotechnology* 29, 244005
76. Filinchuk, Y. *et al.* (2014) *In situ* diffraction study of catalytic hydrogenation of $VO_2$: stable phases and origins of metallicity. *J. Am. Chem. Soc.* 136, 8100–8109
77. Rao, C.N.R. *et al.* (1973) Semiconductor–metal transitions in $NbO_2$ and $Nb_{1-x}V_xO_2$. *J. Solid State Chem.* 6, 340–343
78. Rana, R. *et al.* (2019) Nonthermal nature of photoinduced insulator-to-metal transition in $NbO_2$. *Phys. Rev. B* 99, 041102
79. O'Hara, A. and Demkov, A.A. (2015) Nature of the metal-insulator transition in $NbO_2$. *Phys. Rev. B* 91, 094305
80. Slesazeck, S. *et al.* (2015) Physical model of threshold switching in $NbO_2$ based memristors. *RSC Adv.* 5, 102318–102322
81. Funck, C. *et al.* (2016) Multidimensional simulation of threshold switching in $NbO_2$ based on an electric field triggered thermal runaway model. *Adv. Electron. Mater.* 2, 1600169
82. Gibson, G.A. *et al.* (2016) An accurate locally active memristor model for S-type negative differential resistance in $NbO_x$. *Appl. Phys. Lett.* 108, 023505
83. Pershin, Y.V. and Di Ventra, M. (2011) Memory effects in complex materials and nanoscale systems. *Adv. Phys.* 60, 145–227
84. Pickett, M.D. and Stanley Williams, R. (2012) Sub-100 fJ and sub-nanosecond thermally driven threshold switching in niobium oxide crosspoint nanodevices. *Nanotechnology* 23, 215202
85. Cho, J. *et al.* (2019) The middle road less taken: electronic-structure-inspired design of hybrid photocatalytic platforms for solar fuel generation. *Acc. Chem. Res.* 52, 645–655
86. Parija, A. *et al.* (2016) Topochemically de-intercalated phases of $V_2O_5$ as cathode materials for multivalent intercalation batteries: a first-principles evaluation. *Chem. Mater.* 28, 5611–5620

87. Guo, H. *et al.* (2018) Antiferromagnetic correlations in the metallic strongly correlated transition metal oxide $LaNiO_3$. *Nat. Commun.* 9, 43
88. Nikulin, I.V. *et al.* (2004) Oxygen nonstoichiometry of $NdNiO_{3-\delta}$ and $SmNiO_{3-\delta}$. *Mater. Res. Bull.* 39, 775–791
89. Xuan, X.F. *et al.* (2013) Controlling the sharpness of room-temperature metal–insulator transition in epitaxial $Sm_{0.5}Nd_{0.5}NiO_3$ films. *AIP Adv.* 3, 062133
90. Alonso, J.A. *et al.* (1999) Charge disproportionation in $RNiO_3$ perovskites: simultaneous metal–insulator and structural transition in $YNiO_3$. *Phys. Rev. Lett.* 82, 3871–3874
91. Huang, H. *et al.* (2014) The effect of growth oxygen pressure on the metal–insulator transition of ultrathin $Sm_{0.6}Nd_{0.4}NiO_{3-\delta}$ epitaxial films. *RSC Adv.* 4, 55082–55086
92. Liao, Z. *et al.* (2018) Metal–insulator-transition engineering by modulation tilt-control in perovskite nickelates for room temperature optical switching. *Proc. Natl. Acad. Sci. U. S. A.* 115, 9515–9520
93. Liu, J. *et al.* (2013) Heterointerface engineered electronic and magnetic phases of $NdNiO_3$ thin films. *Nat. Commun.* 4, 2714
94. Heo, S. *et al.* (2016) Modulation of metal–insulator transitions by field-controlled strain in $NdNiO_3/SrTiO_3$/PMN-PT (001) heterostructures. *Sci. Rep.* 6, 22228
95. Alonso, J.A. *et al.* (1999) Metal–insulator transitions, structural and microstructural evolution of RNiO3 (R = Sm, Eu, Gd, Dy, Ho, Y) perovskites: evidence for room-temperature charge disproportionation in monoclinic $HoNiO_3$ and $YNiO_3$. *J. Am. Chem. Soc.* 121, 4754–4762
96. Medarde, M. *et al.* (2008) Long-range charge order in the low-temperature insulating phase of $PrNiO_3$. *Phys. Rev. B* 78, 212101
97. Medarde, M. *et al.* (2009) Charge disproportionation in $RNiO_3$ perovskites (R=rare earth) from high-resolution X-ray absorption spectroscopy. *Phys. Rev. B* 80, 245105
98. Staub, U. *et al.* (2002) Direct observation of charge order in an epitaxial $NdNiO_3$ film. *Phys. Rev. Lett.* 88, 126402
99. Mercy, A. *et al.* (2017) Structurally triggered metal–insulator transition in rare-earth nickelates. *Nat. Commun.* 8, 1677
100. Balachandran, P.V. and Rondinelli, J.M. (2013) Interplay of octahedral rotations and breathing distortions in charge-ordering perovskite oxides. *Phys. Rev. B* 88, 054101
101. Shamblin, J. *et al.* (2018) Experimental evidence for bipolaron condensation as a mechanism for the metal–insulator transition in rare-earth nickelates. *Nat. Commun.* 9, 86
102. Green, R.J. *et al.* (2016) Bond disproportionation and dynamical charge fluctuations in the perovskite rare-earth nickelates. *Phys. Rev. B* 94, 195127
103. Khomskii, D. (1997) Unusual valence, negative charge-transfer gaps and self-doping in transition-metal compounds. *Lith. J. Phys.* 37, 65
104. Mizokawa, T. *et al.* (1991) Origin of the band gap in the negative charge-transfer-energy compound $NaCuO_2$. *Phys. Rev. Lett.* 67, 1638–1641
105. Park, H. *et al.* (2012) Site-selective Mott transition in rare-earth-element nickelates. *Phys. Rev. Lett.* 156402, 156402
106. Bubel, S. *et al.* (2015) The electrochemical impact on electrostatic modulation of the metal–insulator transition in nickelates. *Appl. Phys. Lett.* 106, 122102
107. Marley, P.M. *et al.* (2013) Charge disproportionation and voltage-induced metal–insulator transitions evidenced in β-$Pb_xV_2O_5$ nanowires. *Adv. Funct. Mater.* 23, 153–160
108. Andrews, J.L. *et al.* (2018) Hole extraction by design in photocatalytic architectures interfacing CdSe quantum dots with topochemically stabilized tin vanadium oxide. *J. Am. Chem. Soc.* 140, 17163–17174
109. Andrews, J.L. *et al.* (2018) Reversible Mg-ion insertion in a metastable one-dimensional polymorph of $V_2O_5$. *Chem* 4, 564–585
110. Andrews, J.L. *et al.* (2017) Intercalation-induced exfoliation and thickness-modulated electronic structure of a layered ternary vanadium oxide. *Chem. Mater.* 29, 3285–3294
111. Yamauchi, T. *et al.* (2005) Charge order and superconductivity in vanadium oxides. *Solid State Sci.* 7, 874–881
112. Tolhurst, T. *et al.* (2017) Electronic structure of ε′-$V_2O_5$: an expanded band gap in a double-layered polymorph with increased interlayer separation. *J. Mater. Chem. A* 5, 23694–23703
113. De Jesus, L.R. *et al.* (2016) Mapping polaronic states and lithiation gradients in individual $V_2O_5$ nanowires. *Nat. Commun.* 7, 12022
114. Wangoh, L. *et al.* (2014) Electron lone pair distortion facilitated metal–insulator transition in β-$Pb_{0.33}V_2O_5$ nanowires. *Appl. Phys. Lett.* 104, 182108
115. Onoda, M. and Sato, T. (2017) Polaronic nonmetal-correlated metal crossover system β′-$Cu_xV_2O_5$ with anharmonic copper oscillation and thermoelectric conversion performance. *J. Phys. Soc. Jpn.* 86, 124801
116. Liu, L. *et al.* (2012) New-phase $VO_2$ micro/nanostructures: investigation of phase transformation and magnetic property. *New J. Chem.* 36, 619–625
117. Yao, T. *et al.* (1994) A structural study of the high-temperature phase of $VO_2$(A). *J. Solid State Chem.* 112, 196–198
118. Marezio, M. *et al.* (1972) Structural aspects of the metal–insulator transitions in Cr-doped $VO_2$. *Phys. Rev. B* 5, 2541–2551